Angewandte Chemie
Eine Zeitschrift der Gesellschaft Deutscher Chemiker

Supporting Information

69451 Weinheim, Germany

Sodium Doping Controlled Synthesis of Monodisperse Lanthanide Oxysulfide Ultrathin Nanoplates Guided by Density Functional Calculations**

Yi Ding, Jun Gu, Jun Ke, Ya-Wen Zhang, and Chun-Hua Yan**

anie_201105025_sm_miscellaneous_information.pdf

Supporting Information

Experimentation

A Schlenk line system was utilized in the nanocrystal synthesis. Oleic acid (OA; 90%, Aldrich), oleylamine (OM; > 80%, Acros), 1-octadecene (ODE; >90%, Acros), Ln_2O_3 (Ln = La to Lu, Y), sulfur powders (S; A. R. grade), acetylacetone (Hacac; A. R. grade), nitric acid (HNO_3; A. R. grade), ammonia ($NH_3 \bullet H_2O$; A. R. grade), acetic acid (HAc; > 99.5%), sodium hydroxide (NaOH; > 96%), absolute ethanol (C_2H_6O; > 99.7%), cyclohexane (C_6H_{12}; > 99.5%) were used as received.

Preparation of $Ln(acac)_3$ precursors. Rare-earth acetylacetonate ($Ln(acac)_3$, Ln = La to Lu, Y) was prepared by following the procedure described in Ref. S1.

Preparation of Na(acac) precursor. Sodium acetylacetonate was prepared by following the procedure described in Ref. S2.

Syntheses of Na-doped Ln_2O_2S nanocrystals. In a typical synthesis, $La(acac)_3$ (0.5 mmol), Na(acac) (0.5 mmol), S (0.5 mmol), OA (2.5 mmol), OM (17 mmol), ODE (20 mmol) were loaded in a three-neck flask (100 mL) at RT. The mixture was heated to 120°C under vacuum for 30 min to remove water and other impurities with low boiling points. Meanwhile the La-oleate and Na-oleate complex were formed upon this degassing procedure. The solution was then heated to 310°C at a heating rate of 20 $°C \cdot min^{-1}$ under a high purified N_2 atmosphere. The solution generally turned from turbid to transparent at about 240°C during the heat-up process. After 30 min of reaction, the solution was air-cooled to RT and NCs were precipitated from the crude solution by ethanol, followed by centrifugation and dispersion in cyclohexane. Finely adjusting the amount of Na(acac) would lead to different thickness and size of the nanoplates. Furthermore, when OA were increased from 2.5 mmol to 5 mmol while maintaining the amount of all the other components, the solution would turn milky when kept at 310°C for 10 min. The as-synthesized NCs would self-assemble in solution, forming NWs of several hundred nanometers.

Other Na-doped Ln_2O_2S nanocrystals (Ln = Pr, Nd, Sm, Eu, Gd, Tb) were prepared with the same procedure, except for the use of different $Ln(acac)_3$ precursors, respectively.

The further doping of Eu or Tb in Na-doped La_2O_2S NCs was also realized with the same procedure, except for the additional use of $Eu(acac)_3$ or $Tb(acac)_3$ as precursors, respectively. The doping concentrations of Eu^{3+} and Tb^{3+} are based on the total amount of the lanthanides, and are chosen in accordance with the mostly-used commercial bulk phosphors, respectively.

Syntheses of Bulk La_2O_2S:Eu/Tb Powders. Bulk La_2O_2S:Eu and La_2O_2S:Tb powders were prepared through a modified route described in Ref. S3.

Instrumentation

XRD. Wide Angle X-ray diffraction (WAXRD) patterns of the dry powders were characterized on a Rigaku D/MAX-2000 diffractometer (Japan) with a slit of 1/2 ° at a scanning speed of 2 ° min^{-1} using Cu K_α radiation (λ = 1.5406 Å). Small Angle XRD (SAXRD) measurements were performed on the same instrument with a slit of 1/6 ° at a scanning speed of 1 ° min^{-1}.

TEM, HRTEM & EDS. Samples for transmission electron microscopy (TEM) analysis were prepared by drying a drop of diluted colloid solution of Na-doped La_2O_2S nanocrystals in cyclohexane on copper grids coated by amorphous carbon. For self-assembly on liquid-air interface, samples were prepared according to the procedure described in Ref. S4. High

resolution TEM (HRTEM) and energy dispersive X-ray spectroscopy (EDS) analyses were performed on a FEG-TEM (JEM-2100F, JEOL, Japan) operated at 200 kV. Particle sizes are counted from at least 100 nanocrystals.

ICP-AES. The as-prepared Na-doped La_2O_2S NCs were washed by cyclohexane/ethanol mixed solution and then dissolved in HNO_3/HCl mixed solution. The as-obtained dissolved NCs were subsequently analyzed using a Leeman Labs, Inc., inductively coupled plasma atomic emission spectrometer (ICP-AES) instrument.

XPS. The XPS analysis of the Na-doped La_2O_2S NCs was performed on an ESCALAB5 system. For the exact determination of the core level binding energies, the spectrometer was calibrated with C 1s at 284.6 eV.

FT-IR. FT-IR analyses of the as-prepared samples, as well as the surfactant solutions were performed on a Bruker Vector22 FTIR spectrometer.

DLS. The DLS size distribution characterizations of the as-formed nanoplate superlattice dispersions in cyclohexane were performed on an ALV/DLS/SLS-5022F goniometer system with incident laser (632.8 nm) at a scattering angle of 90°.

Photoluminescence. The UV-simulated photoluminescence properties of as-prepared Na-doped La_2O_2S:Eu and La_2O_2S:Tb NCs at RT were measured on a Hitachi F-4500 fluorescence spectrophotometer (Japan) with a Xenon lamp as a stimulation source. The scanning speed was fixed at 60 nm·min^{-1} with both the excitation and emission splits fixed at 2.5 nm. The lifetime measurements of the nanoplates and the corresponding bulk powders were obtained on an Edinburgh Instruments FLS920 transient/steady-state fluorescence spectrometer at room temperature. The PL quantum yields of the nanocrystals and bulk material were measured by the absolute method using integrating sphere of Horiba Jobin Yvon Nanolog system. The coordinations in the *xy*-chromaticity diagram are directly calculated from the fluorescent spectra (CIE 1931).

Supplementary Data

Similar to previous work reported by Peng et al., (Ref. S5) our EDS and XPS characterizations (Table S1) indicated that the two basal planes of the nanoplates along the <001> direction were both terminated with La^{3+} ions (Figure S4). This is because the cation to S^{2-} anion ratio, i. e. ($[Na^+]+[La^{3+}]$)/$[S^{2-}]$ should be 2:1 if (001) facets are terminated by La^{3+} and (00-1) facets by S^{2-}. However, our elemental analysis showed that the cation to S^{2-} anion ratio is approximately 3:1. This is much higher than the stoichiometric ratio of 2:1, and in good accordance with the 2 layers of S^{2-} and 6 layers of cations in the ultrathin nanoplates composed of 3 primitive cells along the <001> direction (Figure S4b). This ratio also excludes the possibility of $V_S^{\bullet\bullet}$ formation (Table S1), indicating that the major defect should be $V_O^{\bullet\bullet}$ upon Na-doping.

Table S1. Elemental analysis of the as-synthesized Na-doped La_2O_2S NCs, with La_2O_3 NCs synthesized in the absence of S powder as a reference [a)]

Measurement	Molar Ratio				
	La_2O_2S NCs			La_2O_3 NCs[d)]	
	Na	La	S[c)]	Na	La
In Precursor[b)]	50 %	50 %	50 %	50 %	50 %
EDS	21±3 %	79±3 %	30±5 %	9±2 %	91±2 %
XPS	17±3 %	83±3 %	29±6 %	7±3 %	93±3 %
ICP-AES	26±4 %	73±4 %	-	11±4 %	89±4 %

a) The molar ratio is normalized so that $n(Na^+) + n(La^{3+}) = 100\%$. The value of S is therefore calculated as $n(S^{2-})/[n(Na^+) + n(La^{3+})]$.

b) This row indicates the molar ratio of the precursors added in the OA/OM/ODE solution.

c) The EDS and XPS result suggest that: i) each of nanoplates were terminated with 2 layers of La (doped with Na) as basal (001) planes, since each nanoplate contains 2 layers of S and 6 layers of La (doped with Na), the molar ratio of Na, La and S should satisfy the following equation: $n(S^{2-})/[n(Na^+) + n(La^{3+})] \approx 1{:}3$; ii) If as-formed vacancies were sulfur vacancies, the following equation should be satisfied: $n(S^{2-})/[n(La^{3+}) - 2n(Na^+)] \approx 1{:}3$, which is far from our elemental analysis results, indicating that the formation of sulfur vacancies can be excluded.

d) The synthesis of La_2O_3 NCs can also serve as the control experiment in order to show the reliability of these three methods of elemental analysis. (TEM images refer to Figure S2)

Table S2. Sizes of the as-synthesized Na-doped $La_2O_2S:Eu^{3+}$ and Na-doped $La_2O_2S:Tb^{3+}$ nanoplates.

Precursors [a)]	T/°C	t/min	Size/nm
$Eu(acac)_3$ 0.02 mmol	310	30	$(2.1 \pm 0.2) \times (25.5 \pm 3.5)$
$Tb(acac)_3$ 0.005 mmol	310	30	$(2.4 \pm 0.4) \times (27.5 \pm 4.5)$

a) Other precursors were maintained as: 0.5 mmol of $La(acac)_3$, 0.5 mmol of Na(acac), 5 mmol of OA, 17 mmol of OM, 20 mmol of ODE.

Table S3. Observed 2θ values from the XRD pattern of the Na-doped La_2O_2S NCs, compared with the standard reference (JCPDS 27-0263)

Observed[a)]	Standard	(hkl)
25.33	25.35	(100)
28.37	28.51	(101)
36.22	36.34	(102)
44.62	44.74	(110)
46.16	46.84	(103)
52.01	52.69	(004)
53.70	53.87	(201)

a) The refined lattice parameters of the Na-doped La_2O_2S NCs are: $a = b = 4.06$ Å, $c = 7.04$ Å (For bulk La_2O_2S of the standard reference: $a = b = 4.05$ Å, $c = 6.94$ Å).

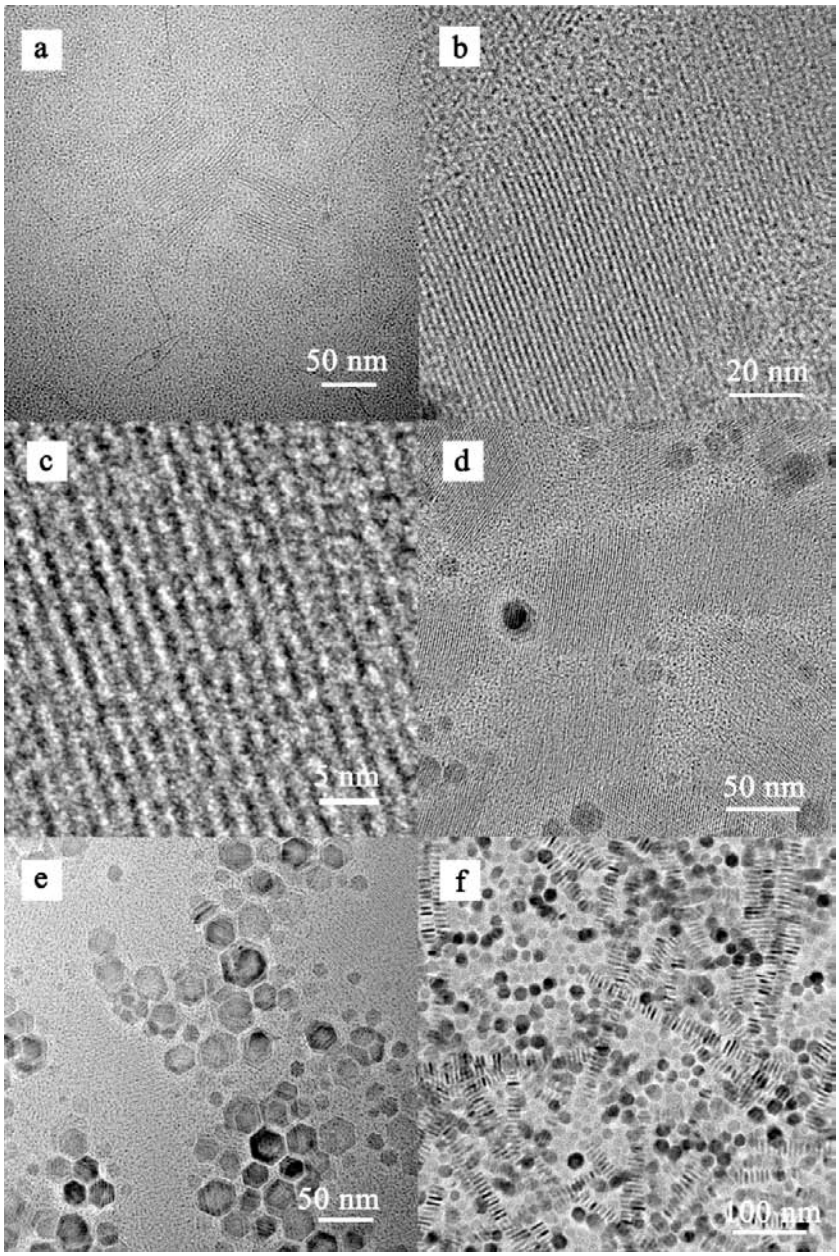

Figure S1. TEM images of as-synthesized samples with different amounts of Na(acac) under the conditions that the other synthetic parameters were fixed as 0.5 mmol of $La(acac)_3$, 1 mmol of S powder, 2.5 mmol of OA, 17 mmol of OM, 20 mmol of ODE: a) no Na(acac) precursor was added; b) high magnification of the nanowires in panel a; c) HRTEM image of the nanowires, in which the NWs show no HRTEM fringes; d) 0.1 mmol of Na(acac); e) 0.2 mmol of Na(acac); f) 0.5 mmol of Na(acac). The doping content of Na^+ ion in the La_2O_2S NCs could be finely tuned when changing the molar ratio between the precursors La(acac) and Na(acac). From EDS analysis, the as-determined Na content nearly linearly increases from 4.4% (panel d), to 8.3% (panel e), and to 21% (panel f) with the amount of Na(acac) added (from 0.1, to 0.2 and to 0.5 mmol). It was also found that the increasing amount of Na(acac) in the precursors not only change the sizes of the NCs, and can lead to much better monodispersity for the Na-doped NCs. Furthermore, our preliminary results show that the change of doping concentration of Na^+ ions can affect the red emissions of Eu^{3+} ions in the Na,Eu co-doped La_2O_2S NCs, which deserves our on-going investigation.

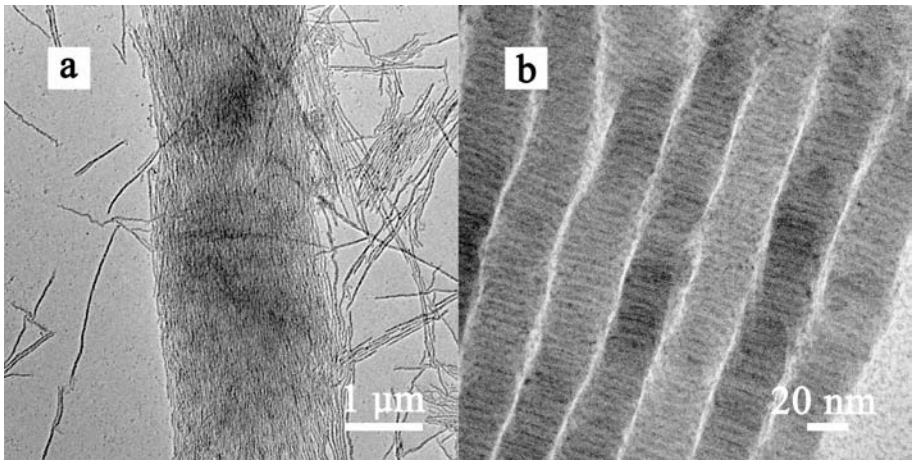

Figure S2. a) Low magnification and b) high magnification TEM images of the as-synthesized La_2O_3 NCs from the control experiment (precursors were 0.5 mmol of $La(acac)_3$, 0.5 mmol of Na(acac) and solvents were 2.5 mmol of OA, 17 mmol of OM, 20 mmol of ODE).

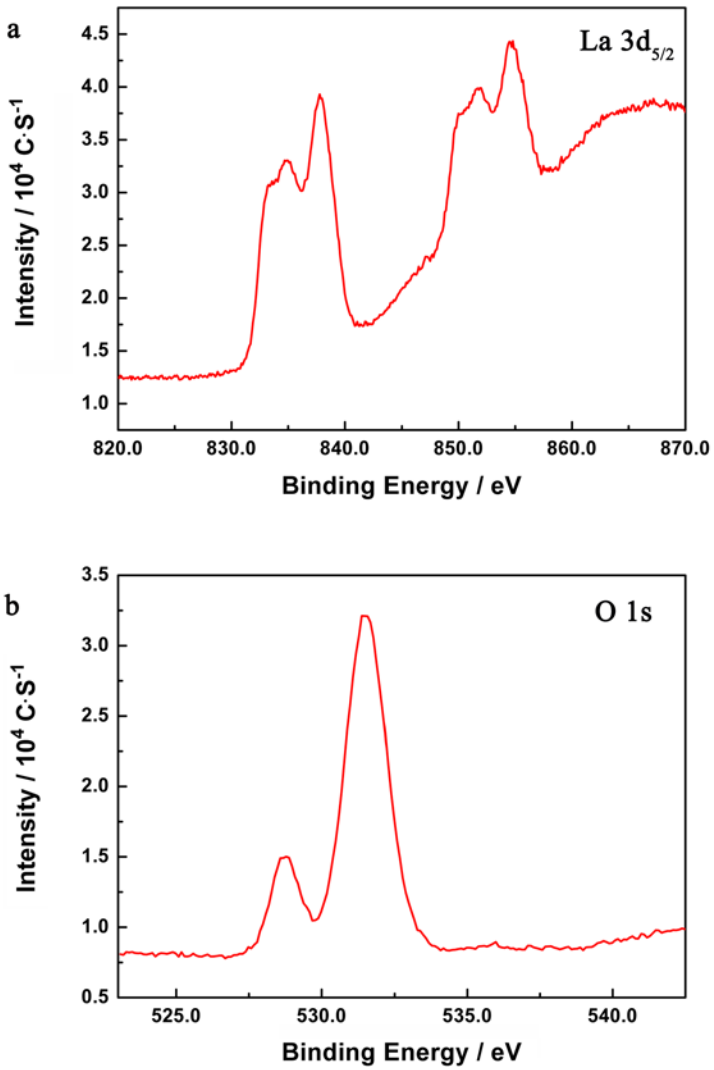

Figure S3. XPS spectra of a) La ($3d_{5/2}$) and b) O(1s) of the as-synthesized Na-doped La_2O_2S NCs. Compared with the bulk sample, the peaks of O(1s) has shifted 0.5 eV towards higher energy (i.e. from 531.4 eV to 531.9 eV). According to the XPS data, the molar ratio between O and La of the Na-doped La_2O_2S NCs is calculated to be 0.72 : 1, while the molar ratio between O and La of the bulk La_2O_2S is calculated to be 0.93 : 1. This characterization also indicates that the formation of oxygen vacancy upon Na-doping.

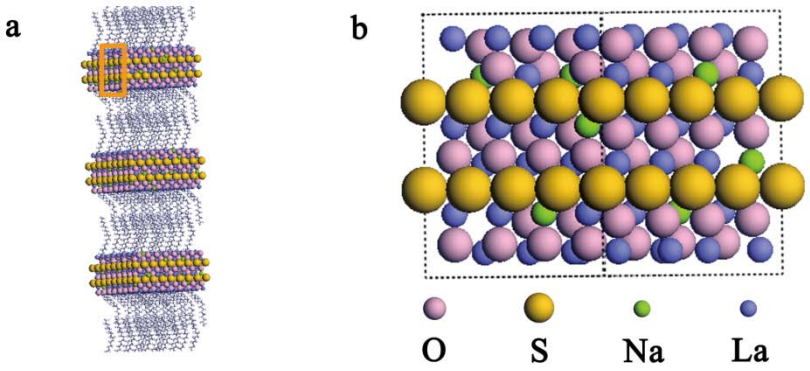

Figure S4. a) Schematic illustration for self-assembled Na-doped La_2O_2S nanoplates with OA as capping agents; the orange box highlighted in a) is enlarged in b), which shows the thickness of one nanoplate, indicating the three layers of primitive cells along *c*-axis with La^{3+} as ending ions on both sides of the nanoplates.

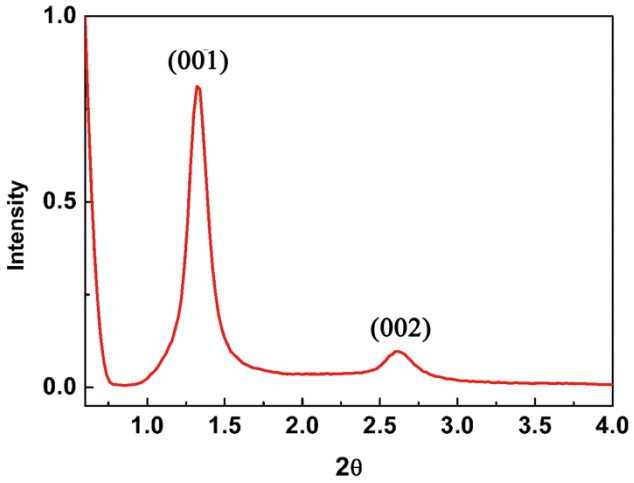

Figure S5. Small angle XRD pattern of the self-assembled Na-doped La_2O_2S nanoplates.

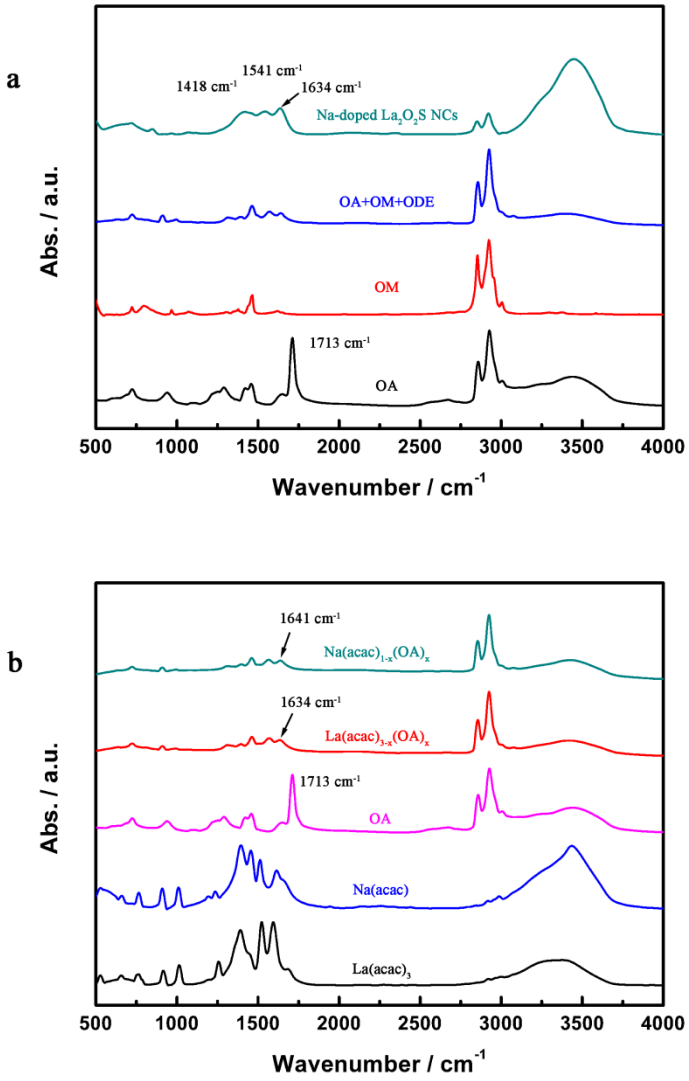

Figure S6. a) FT-IR spectra of Na-doped La_2O_2S nanoplates, mixture of OA/OM/ODE (OA : OM :ODE = 5 mmol : 17 mmol : 20 mmol), sole OA, and sole OM. The shift of the ν_{CO} vibrations from the free OA molecules to the washed Na-doped La_2O_2S nanoplates (from 1713 cm^{-1} to 1641 cm^{-1}) confirmed the formation of coordination bonds between carboxylic groups of OA molecules with cations on the surfaces of the nanoplates; b) FT-IR spectra of different precursors. The formation of $La(acac)_{3-x}(OA)_x$ and $Na(acac)_{1-x}(OA)_x$ complexes during the thermal treatment of $La(acac)_3$ and Na(acac) precursors in the mixed solution of OA/OM/ODE ($La(acac)_3$: OA : OM : ODE = 0.5 mmol : 5 mmol : 17 mmol : 20 mmol, Na(acac) : OA : OM : ODE = 0.5 mmol : 5 mmol : 17 mmol : 20 mmol, respectively, degassed at 110 °C for 15 min) is indicated by the shift of the ν_{CO} vibrations from 1713 cm^{-1} to 1641 cm^{-1} and 1634 cm^{-1}, respectively. (Ref. S6)

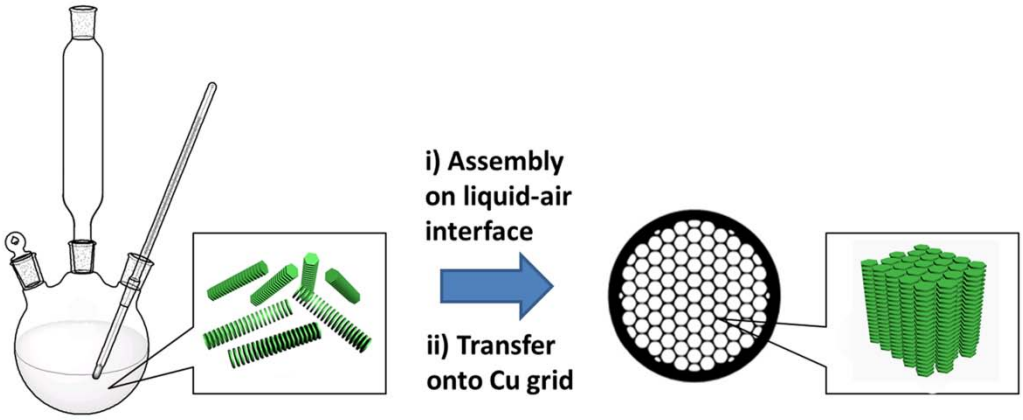

Figure S7. Schematic representation of the assembled Na-doped La_2O_2S nanoplates in solution forming hexagonal closed-packed perpendicularly aligned NW arrays on copper grids coated by amorphous carbon.

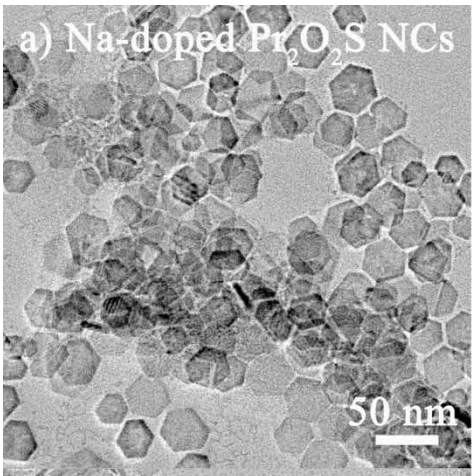
a) Na-doped Pr_2O_2S NCs
50 nm

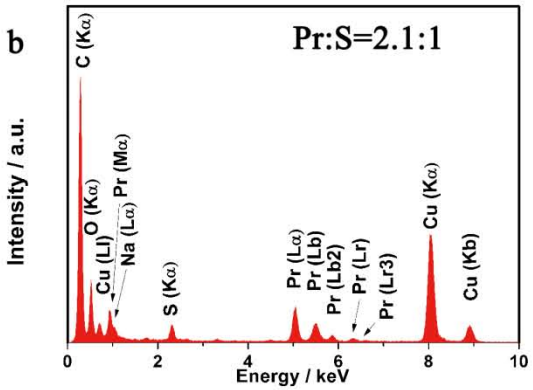
b
Pr:S=2.1:1
Intensity / a.u.
Energy / keV
C (Kα)
O (Kα)
Cu (Ll)
Na (Lα)
Pr (Mα)
S (Kα)
Pr (Lα)
Pr (Lb)
Pr (Lb2)
Pr (Lr)
Pr (Lr3)
Cu (Kα)
Cu (Kb)

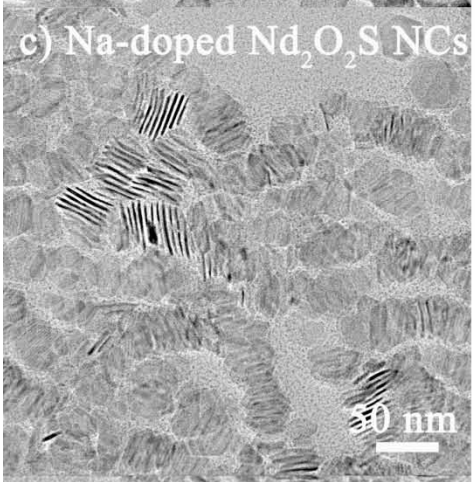
c) Na-doped Nd_2O_2S NCs
50 nm

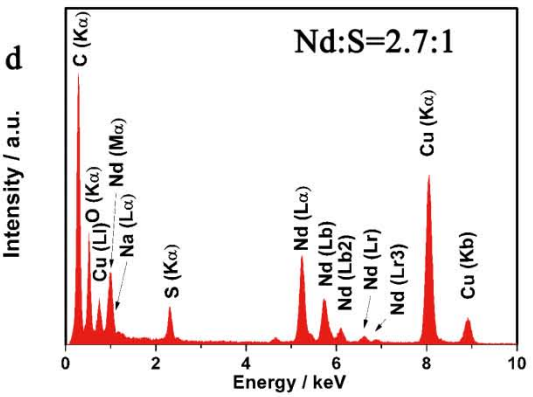
d
Nd:S=2.7:1
Intensity / a.u.
Energy / keV
C (Kα)
O (Kα)
Cu (Ll)
Na (Lα)
Nd (Mα)
S (Kα)
Nd (Lα)
Nd (Lb)
Nd (Lb2)
Nd (Lr)
Nd (Lr3)
Cu (Kα)
Cu (Kb)

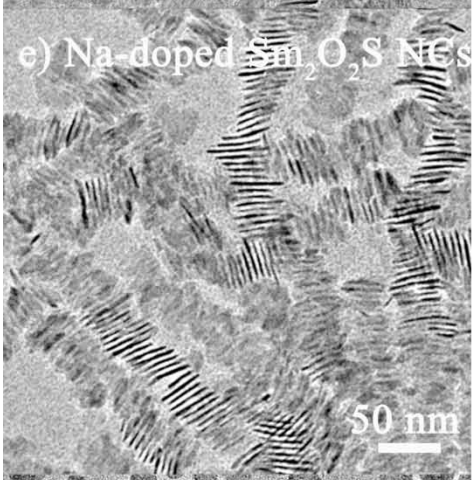
e) Na-doped Sm_2O_2S NCs
50 nm

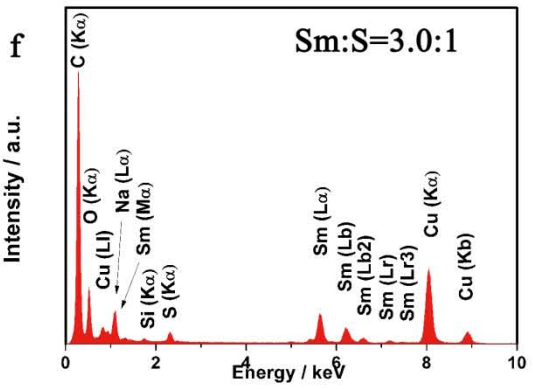
f
Sm:S=3.0:1
Intensity / a.u.
Energy / keV
C (Kα)
O (Kα)
Cu (Ll)
Na (Lα)
Sm (Mα)
Si (Kα)
S (Kα)
Sm (Lα)
Sm (Lb)
Sm (Lb2)
Sm (Lr)
Sm (Lr3)
Cu (Kα)
Cu (Kb)

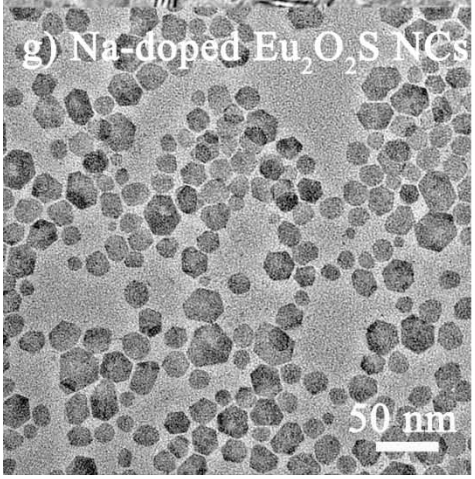
g) Na-doped Eu_2O_2S NCs
50 nm

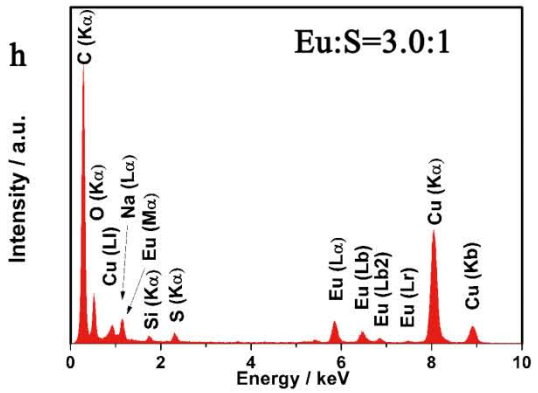
h
Eu:S=3.0:1
Intensity / a.u.
Energy / keV
C (Kα)
O (Kα)
Cu (Ll)
Na (Lα)
Eu (Mα)
Si (Kα)
S (Kα)
Eu (Lα)
Eu (Lb)
Eu (Lb2)
Eu (Lr)
Cu (Kα)
Cu (Kb)

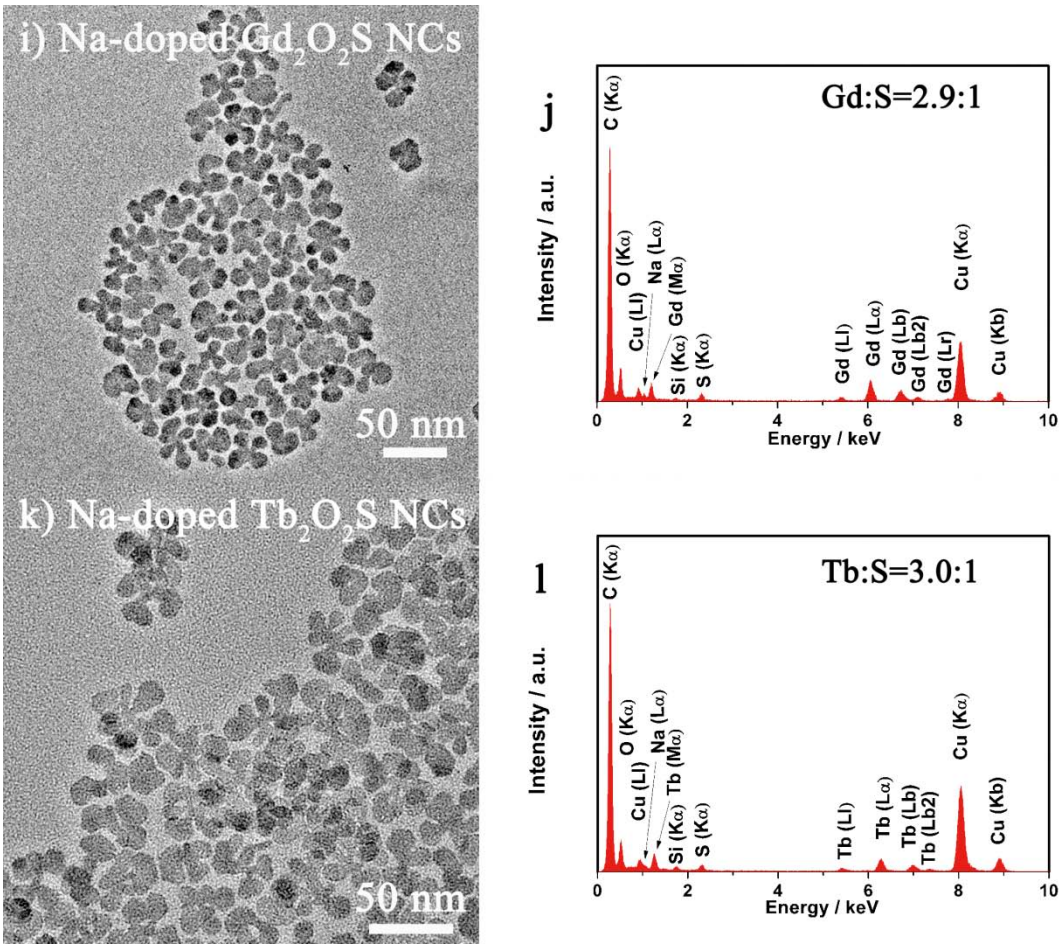

Figure S8. a to l) TEM images and corresponding EDS spectra of different Ln_2O_2S NCs (Ln = Pr, Nd, Sm, Eu, Gd, Tb). Since in octahedral coordination geometry, r_{Na}^{+} = 1.02 Å, r_{La}^{3+} = 1.03 Å and r_{Ln}^{3+} decreases along Ln series (r_{Tb}^{3+} = 0.92Å), the doping efficiency decreases along Ln series. Therefore the mismatch in ionic radii eventually causes insufficient Na-doping, leading to the fact that Na-doped Ln_2O_2S NCs for heavy lanthanides (Ln = Y, Dy-Lu) could not be synthesized by this method.

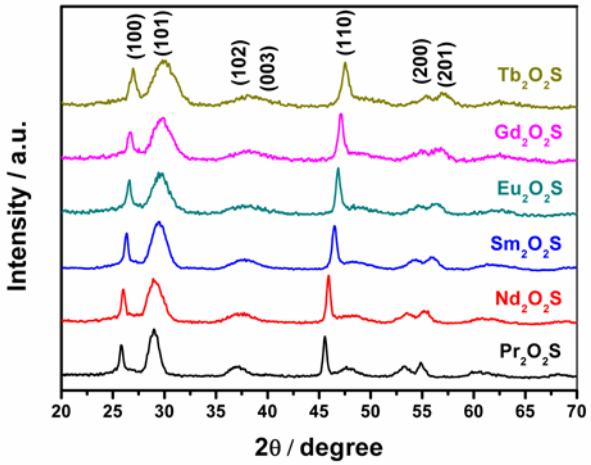

Figure S9. XRD patterns of different Na-doped Ln_2O_2S NCs (Ln = Pr, Nd, Sm, Eu, Gd, Tb; "Na-doped" is not indicated in the figure for simplicity).

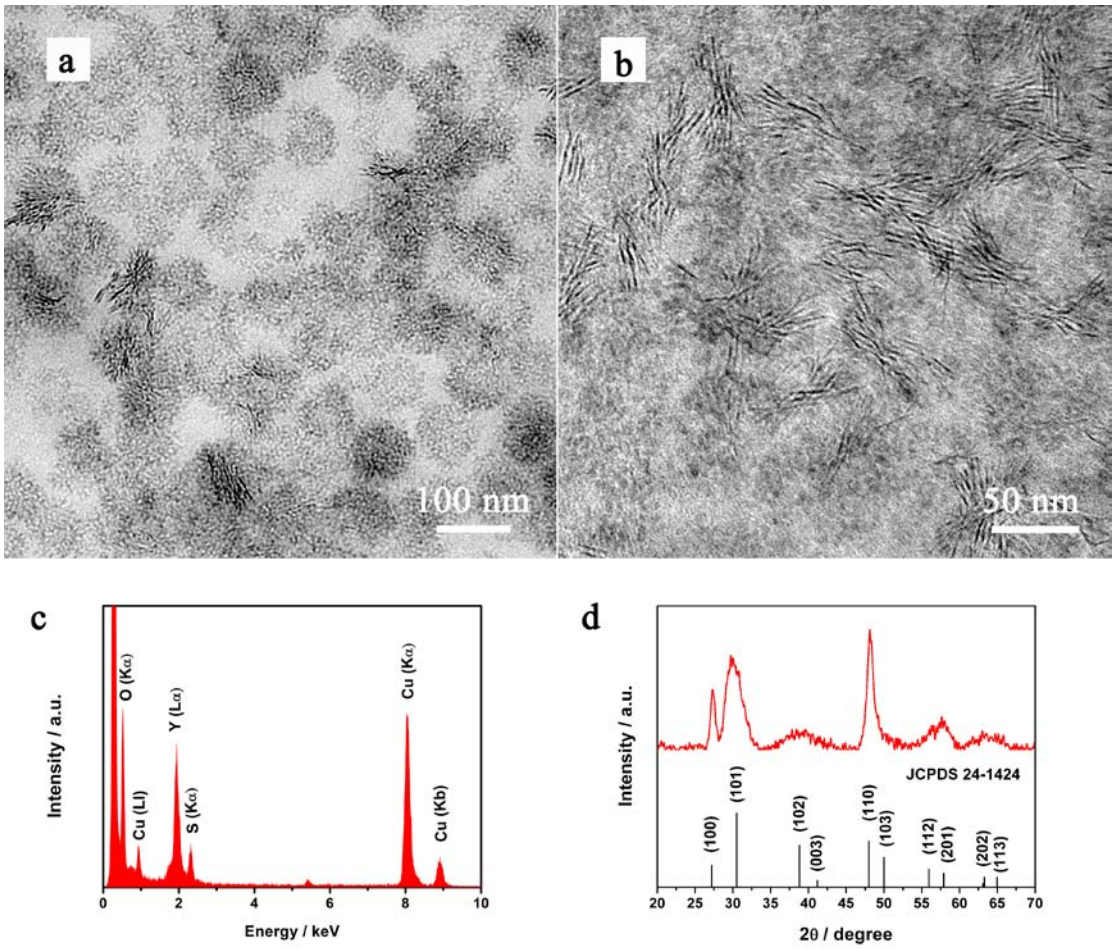

Figure S10. a) Low magnification and b) high magnification TEM images of the as–synthesized Li-doped Y_2O_2S nanoplates; c) corresponding EDS spectrum and d) XRD pattern.

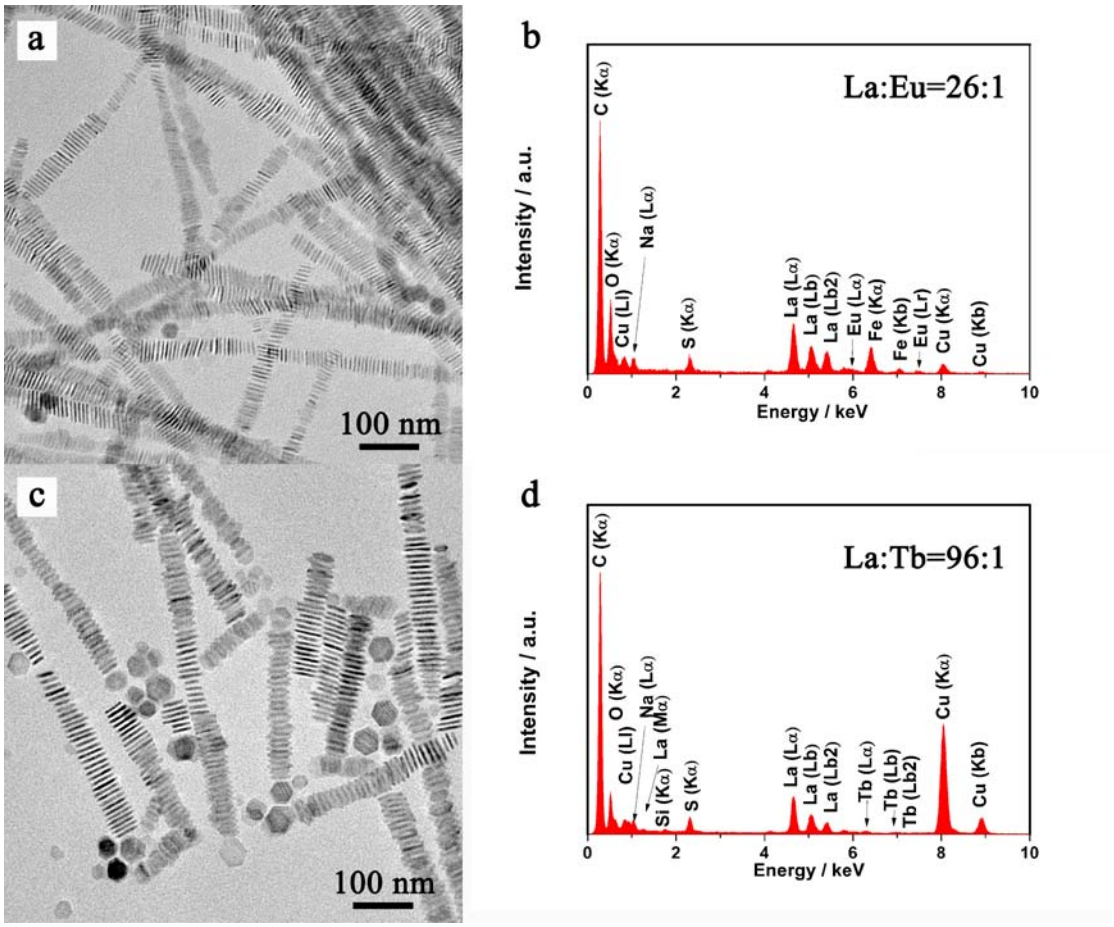

Figure S11. TEM image a) and corresponding EDS spectrum b) of Na-doped La_2O_2S:4%Eu nanoplates; TEM image c) and corresponding EDS spectrum d) of Na-doped La_2O_2S:1%Tb nanoplates.

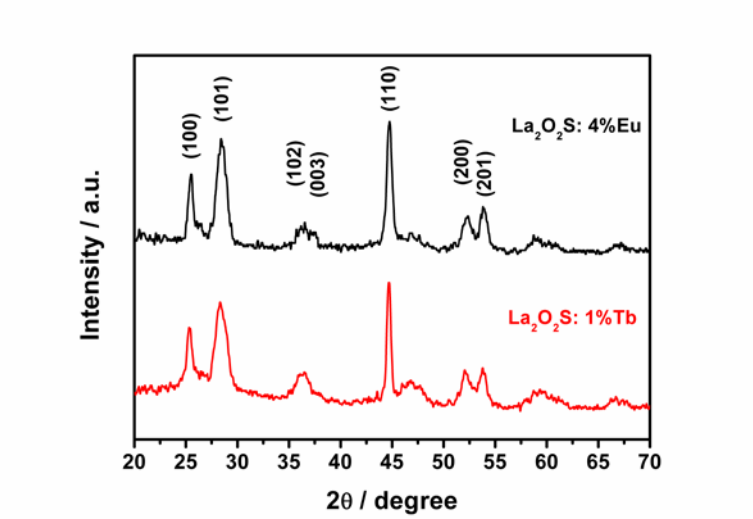

Figure S12. XRD patterns of Na-doped La_2O_2S:4%Eu nanoplates and Na-doped La_2O_2S:1%Tb nanoplates. ("Na-doped" is not indicated in the figure for simplicity)

.

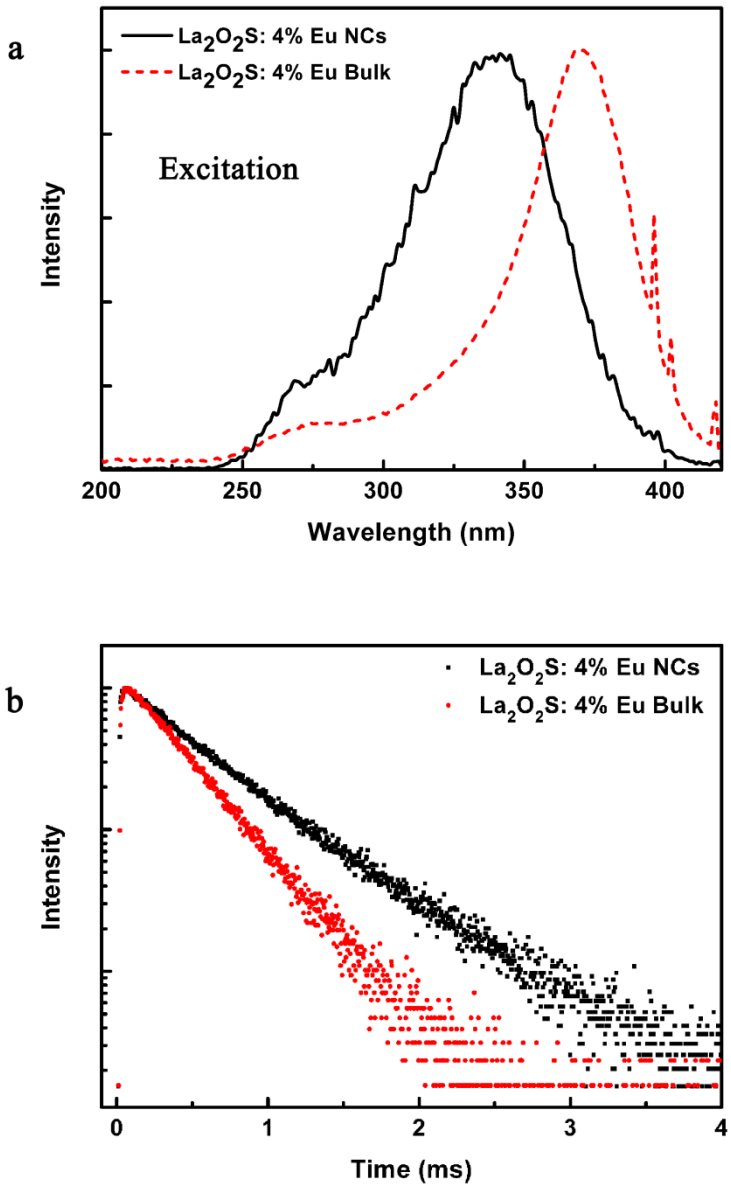

Figure S13. a) Room temperature excitation spectra of Na-doped La_2O_2S:4%Eu nanoplates and its bulk counterpart with emission of 623 nm ("Na-doped" is not indicated in the figure for simplicity). The excitation band from 250 to 300 nm is ascribed to O^{2-} to Eu^{3+} charge transfer, while the broad excitation band above 300 nm is ascribed to S^{2-} to Eu^{3+} charge transfer (Ref. 3d and 3e). Since the nanoplates are terminated by Ln^{3+} on both (001) facets, the amount of S^{2-} in nanoplates is less than bulk material, therefore the S^{2-} to Eu^{3+} charge transfer is not as strong as in bulk material; b) Luminescence decay curves (exponent coordinates is used for intensity axis) of the 623 nm emission of Eu^{3+} ions in Na-doped La_2O_2S:4%Eu nanoplates and bulk material under excitation of 340 nm.

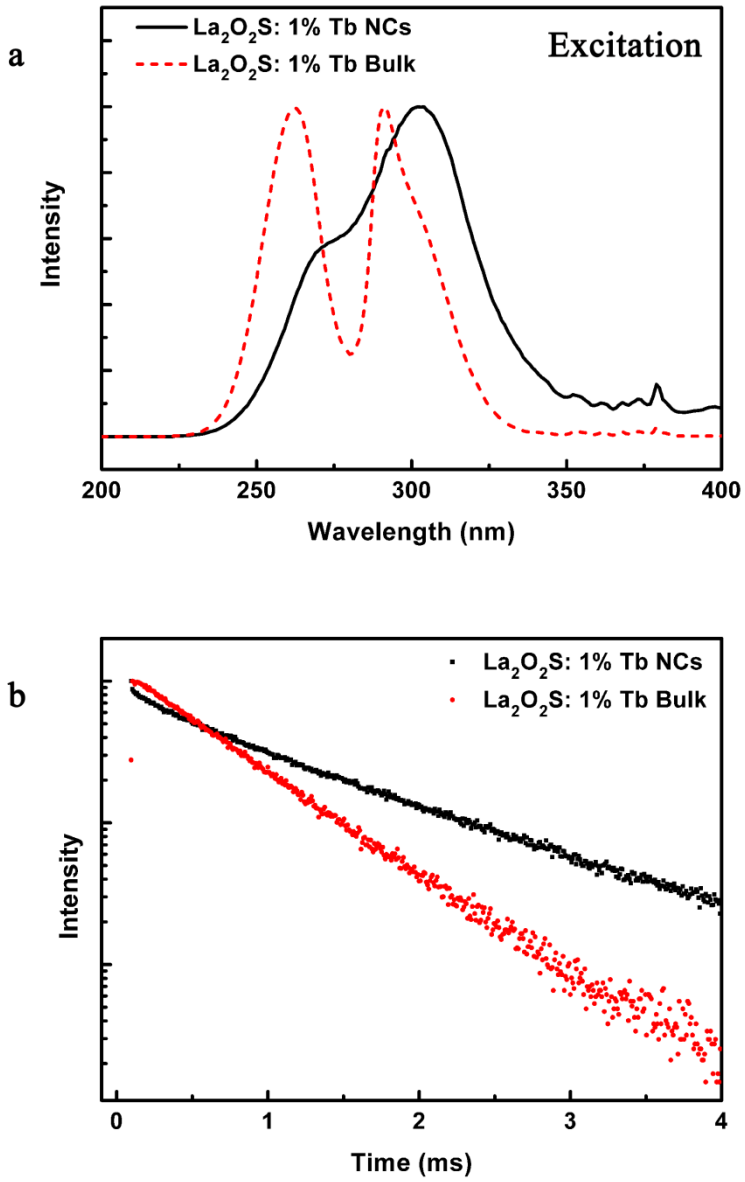

Figure S14. a) Room temperature excitation spectra of La_2O_2S:1%Tb nanoplates and its bulk counterpart with emission of 544 nm ("Na-doped" is not indicated in the figure for simplicity). The excitation band at 260 nm is ascribed to the $4f^8$ to $4f^75d^1$ transition of Tb^{3+} (Ref. 3d), the difference between the nanocrystals and the bulk materials is ascribed to the change in the local crystal field of Tb^{3+}; b) Luminescence decay curves (exponent coordinates is used for intensity axis) of the 544 nm emission of Tb^{3+} ions in La_2O_2S:1%Tb nanoplates and bulk material under excitation of 340 nm.

Density Functional Calculation of Na-doped La_2O_2S

The DFT calculation was performed by using the Vienna Ab-initio Simulation Package (VASP, version 5.2). It was reported in a previous calculation that the GGA and the GGA+U calculations for La_2O_3 system are in quantitative agreement with regard to the vacancy formation energy. (Ref. S7) Therefore we have used GGA throughout our calculation. The DFT calculation included the PBE functional and projector augmented-wave pseudopotentials (PAW). The kinetic energy cut-off for the plane-wave basis set is 450 eV. For the Brillouin zone integration, a 5×5×3 Monkhorst-Pack special k-point mesh is used to calculate the primitive cell of La_2O_2S and La_2O_3, 3×3×3 Monkhorst-Pack special k-point mesh is used to calculate the 2×2×2 supercells. The calculated crystal parameters of bulk La_2O_2S is a = 4.060, c/a = 1.712, which is in good agreement with the experimental values (JCPDS 27-0263, Space Group P-3m1, a = 4.050, c/a = 1.714). (Ref. S8) Other calculated phases include hexagonal La_2O_3 (JCPDS 40-1279, Space Group P-3m1), orthorhombic La_2S_3 (JCPDS 25-1041, Symmetry Group PNMA), hexagonal La (JCPDS 01-0718, Symmetry Group Fm3m), cubic Na (JCPDS 01-0850, Symmetry Group Im-3m), orthorhombic S (JCPDS 08-0247, Symmetry Group Fddd) and one O2 molecule in a 15 Å×15 Å×15 Å box.

The calculated results are summarized in Table S4. In order to calculate the formation energy of the defects, the 2×2×1 supercells were used with all the atoms allowed to relax. The calculated supercell for Na-doped La_2O_2S is therefore $La_7O_8S_3Na$ when $V_S^{\bullet\bullet}$ is formed upon doping of Na^+, $La_7O_7S_4Na$ when $V_O^{\bullet\bullet}$ is formed; and for Na-doped La_2O_3, only $V_O^{\bullet\bullet}$ can be formed, so the calculated formula of the supercell is $La_7O_{11}Na$.

Table S4. Formation energies of different elements and compounds.

	E_{tot}(eV)	μ (eV)
O	– 4.93	0
Na	– 1.29	0
S	– 4.14	0
La	– 4.91	0
La_2O_2S	– 39.8	– 16.1
La_2O_3	– 41.9	– 17.4
La_2S_3	– 132.9	– 11.0
$La_7O_8S_3Na$ V_S	– 144.9	– 57.4
$La_7O_7S_4Na$ V_O	– 142.9	– 56.2
$La_7O_{11}Na$ V_O	– 150.3	– 60.8

The phase diagram (Figure 2) between La_2O_2S and La_2O_3 is calculated based on the following equations:

$$La_2O_2S + O \rightarrow La_2O_3 + S \quad \text{(S1)}$$

$$\mu_O = \mu_S + E_{tot}(La_2O_3) - E_{tot}(La_2O_2S) \quad \text{(S2)}$$

The phase diagram (Figure 4b) between Na-doped La_2O_2S and Na-doped La_2O_3 is calculated based on the following equations:

$$La_7O_8S_3Na + 3O \rightarrow La_7O_7S_4Na + 3S \quad \text{(S3)}$$

$$\mu_O = \mu_S + \frac{1}{3}[E_{tot}(La_7O_7S_4Na) - E_{tot}(La_7O_8S_3Na)] \quad \text{(S4)}$$

The calculation of Na-doped La_2O_2S and Na-doped La_2O_3 is based on all possible anion vacancy sites upon doping of Na^+. The 2×2×1 supercell crystal lattice of La_2O_2S and La_2O_3 can both be regarded as *hcp*-type layers of La^{3+} ions in hcp-type anion layers (i.e. O^{2-} and S^{2-}),

forming |AcBCb| AcBCb type structure along the <001> direction with uppercase letter being the anion layers and lowercase being cation layers (Figure S15). The Na-doping site is noted in green, and substitute one La^{3+} ion in the layer c. All six possible anion vacancies are noted in Figure S15 and the calculated total energy is summarized in Table S5. The lowest formation energy for each type of anion vacancy is chosen for further analysis (i.e. A2 for $V_S^{\bullet\bullet}$ of La_2O_2S, B2 for $V_O^{\bullet\bullet}$ of La_2O_2S and B1 for $V_O^{\bullet\bullet}$ of La_2O_3).

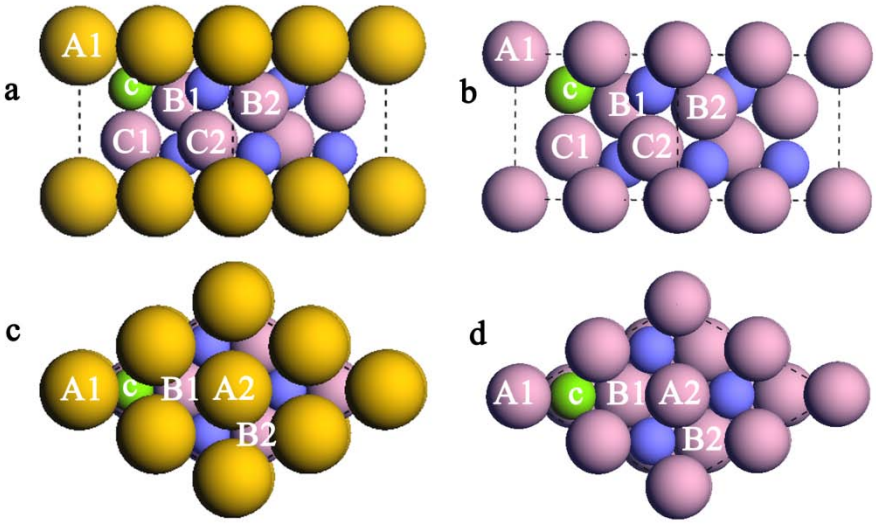

Figure S15. Atomic representations of La_2O_2S along the a) <110> and c) <001> directions. Six possible anion vacancies are noted (i.e. A1, A2, B1, B2, C1, C2, with uppercase letter indicating the corresponding anion layer). Atomic representations of La_2O_3 along the b) <110> and d) <001> directions.

Table S5. Formation energies of different supercells with defects.

anion vacancy site	La_2O_2S		La_2O_3	
	E_{tot} (eV)	type of vacancy	E_{tot} (eV)	type of vacancy
A1	– 144.9	$V_S^{\bullet\bullet}$	– 149.4	$V_O^{\bullet\bullet}$
A2	– 144.4	$V_S^{\bullet\bullet}$	– 148.4	$V_O^{\bullet\bullet}$
B1	– 142.9	$V_O^{\bullet\bullet}$	– 150.3	$V_O^{\bullet\bullet}$
B2	– 142.2	$V_O^{\bullet\bullet}$	– 149.6	$V_O^{\bullet\bullet}$
C1	– 142.6	$V_O^{\bullet\bullet}$	– 149.6	$V_O^{\bullet\bullet}$
C2	– 142.3	$V_O^{\bullet\bullet}$	– 150.0	$V_O^{\bullet\bullet}$

[S1] J. G. Stites, C. N. McCarty, L. L. Quill, *J. Am. Chem. Soc.* **1948**, 70, 3142.
[S2] R. Charles, *Organic Syntheses, Coll.* **1963**, 4, 869; **1959**, 39, 61.
[S3] F. Y. Guo, Z. P. Huang, *Acta Scicentiarum Naturalum Universitis Pekinesis* **1982**, 5, 81.
[S4] A. G. Dong, J. Chen, P. M. Vora, J. M. Kikkawa, C. B. Murray, *Nature* **2010**, 466, 474.
[S5] Z. Li, X. G. Peng, *J. Am. Chem. Soc.* **2011**, 133, 6578.
[S6] A. X. Yin, Y. W. Zhang, C. H. Yan, *Chem. Eur. J.* **2011**, 17, 8033.
[S7] B. Li, H. Metiu, *J. Phys. Chem. C* **2010**, 114, 12234.
[S8] K. R. Laud, T. Y. Tien, H. L. Stadler, *J. Am. Ceram. Soc.* **1971**, 54, 530.